Contamination in dielectric barrier discharge plasmas by electrode erosion

Contamination in dielectric barrier discharge plasmas by electrode erosion

Robin De Meyer[1, 2, 3], Jo Verbeeck[2], Sara Bals[2, 3,*] and Annemie Bogaerts[1,*]

[1] *Research group PLASMANT, Department of Chemistry, University of Antwerp, Universiteitsplein 1, 2610 Antwerp, Belgium*
[2] *Research group EMAT, Department of Physics, University of Antwerp, Groenenborgerlaan 171, 2020 Antwerp, Belgium*
[3] *Nanolab Centre of Excellence, University of Antwerp, Groenenborgerlaan 171, 2020 Antwerp, Belgium*

* *corresponding author: annemie.bogaerts@uantwerpen.be*
* *corresponding author: sara.bals@uantwerpen.be*

Abstract

Dielectric barrier discharge plasmas find applications in various fields, including material synthesis and functionalization, plasma catalysis for gas conversion, pollution control, and biological sample treatment. While electrode erosion in these systems has been observed previously, its full implications have remained unclear. In this study, we analyze the effects of electrode erosion by examining alumina spheres exposed to the plasma, using electron microscopy for detailed characterization. Our findings show that that electrode erosion leads to the deposition of microscopic particles on the materials inside the plasma reactor. Whereas the operating parameters influence the properties of these particles, their formation and deposition is persistent. These electrode particles are an evident source of contamination, and may lead to impurities in synthesized materials, or altered plasma discharges after long-term operation. Our study highlights the importance of acknowledging the presence and potential impact of these particles for various DBD plasma applications, and calls for greater awareness in the scientific community regarding this source of contamination that has been overlooked so far.

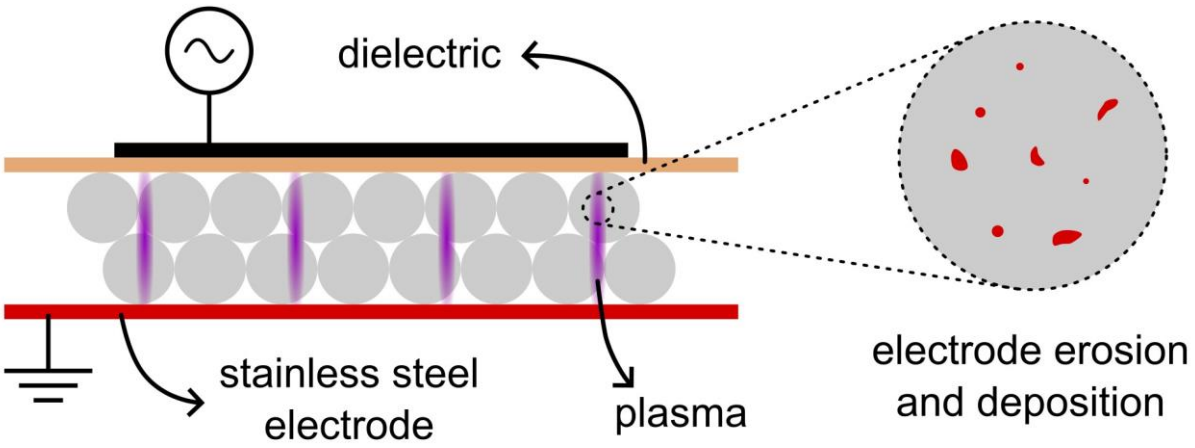

A dielectric barrier discharge (DBD) is a type of plasma ignited between two electrodes, and is characterized by the presence of a dielectric layer covering at least one of the electrodes, preventing persistent high current arcs from being formed. As a result, DBDs are non-equilibrium plasmas, meaning that the gas temperature is several orders of magnitude lower than the electron temperature.[1] These gentle conditions, combined with the reactive nature of the plasma, partially consisting of excited species, radicals, ions, and electrons, offer a great variety of applications, including surface treatment,[2–4] (nano)material synthesis and functionalization,[5–8] catalyst regeneration,[9,10] plasma catalysis for gas conversion and pollution control,[11–13] as well as biological and medical applications.[14–17]

DBDs can operate in various geometries. For many applications, packed-bed DBDs are employed, in which the volume between the electrodes (where the plasma is generated) is filled with a packing material. Indeed, this geometry offers a unique intimate contact between the plasma and the packing material.

Regardless of the geometry, DBDs typically operate in a filamentary mode.[18] This means that generally, the gas volume is not filled with a homogeneous plasma, but rather with discrete filaments. These filaments are formed by so-called microdischarges, i.e., short-lived but intense discharges, which can also be observed in the measured current as sharp peaks, with relatively high current densities (up to 1000 A cm^{-2}). Microdischarges often majorly contribute to the chemistry in a DBD plasma, but given their short lifetime and discrete nature, gas heating remains limited.[18]

The dielectric barrier, especially when employing relatively soft materials, such as polymers, can erode due to the plasma exposure.[19,20] In addition, erosion of the exposed electrode in surface DBDs was previously described.[21–24] For example, recently, Nguyen-Smith et al. observed the erosion of the exposed electrode of a surface DBD after operating in air for 60 minutes.[22] By tuning the pulse width of the applied voltage, the authors managed to operate the plasma both in a filamentary and a relatively uniform mode, while keeping other discharge parameters such as plasma power similar. Detailed scanning electron microscopy (SEM) and energy dispersive X-ray spectroscopy (EDX) measurements revealed that the electrode was measurably eroded in both cases, though significant differences were observed between the electrodes exposed to a filamentary or a homogeneous plasma. The authors reported that a filamentary discharge locally melts the nickel electrode, with some nickel oxide particles being present, both on the electrode, as well as on the dielectric around the eroded area. In contrast, the electrode exposed to a homogeneous discharge did not show any local melting of the electrode. Whereas the oxidation is most likely due to the presence of oxygen, the plasma discharge clearly affects the electrode, and the precise discharge characteristics further determine the extent and nature of the erosion.

Given the demonstrated erosion of the electrode due to the plasma discharge and the apparent mobility of the eroded electrode material, the question arises whether a material inside a DBD could possibly be affected by the eroded electrode material. To answer this question, we employed a coaxial DBD, with an exposed stainless steel electrode passing through the center of an Al_2O_3 cylinder, which has the second electrode wrapped around the outside. A schematic of the setup, as well as further technical details, can be found in the Experimental Methods section in the supporting information (SI, Section S1.1). The reactor was packed with pristine γ-Al_2O_3 spheres (Sasol) with a diameter of 1.8 mm. To investigate the influence of the discharge characteristics, experiments were performed in pure Ar, He, and CO_2. Further, to isolate the effect of temperature on the plasma discharge from any potential changes to the packing material itself, every experiment was performed in two phases. First, the plasma was operated for 3 hours for Ar and He, and for 6 hours for CO_2, after which the plasma was stopped. The reactors were then left to cool down completely, while continuing the gas flow, without further

disturbances. After reaching room temperature, the plasma was operated again for 2 hours in the case of Ar and He, and 3 hours using CO_2 as further discussed below.

After completing the plasma experiment, the used Al_2O_3 spheres were analyzed by SEM and transmission electron microscopy (TEM). The sample preparation procedure and the parameters used for the SEM and TEM analyses are provided in the SI (Section S1.2). In Figure 1, backscattered electron (BSE) SEM images are shown of the surface of the Al_2O_3 spheres exposed to the Ar (A-B), He (C-D), and CO_2 (E-F) plasma. The BSE-SEM signal is proportional to the mass density of the sample, which allows to easily identify heavier (metallic) particles against the lighter Al_2O_3 background. Note that every particle that is shown or included in further analyses, was confirmed to be stainless steel (containing Fe and Cr; and when a high signal to noise ratio was obtained, Ni could also be identified; see SI, Section S2.1) using X-ray based spectroscopy. It stands out that both the Ar sample (Figure 1 A) and the CO_2 sample (Figure 1 E) contain highly spherical stainless steel particles, whereas no such particles were found in the He sample. Further, all samples contain particles of various, seemingly arbitrary, morphology. Moreover, it is striking that the CO_2 sample has a significantly higher fraction of highly spherical particles compared to the Ar sample: 12 out of 19 for CO_2 and 4 out of 24 for Ar.

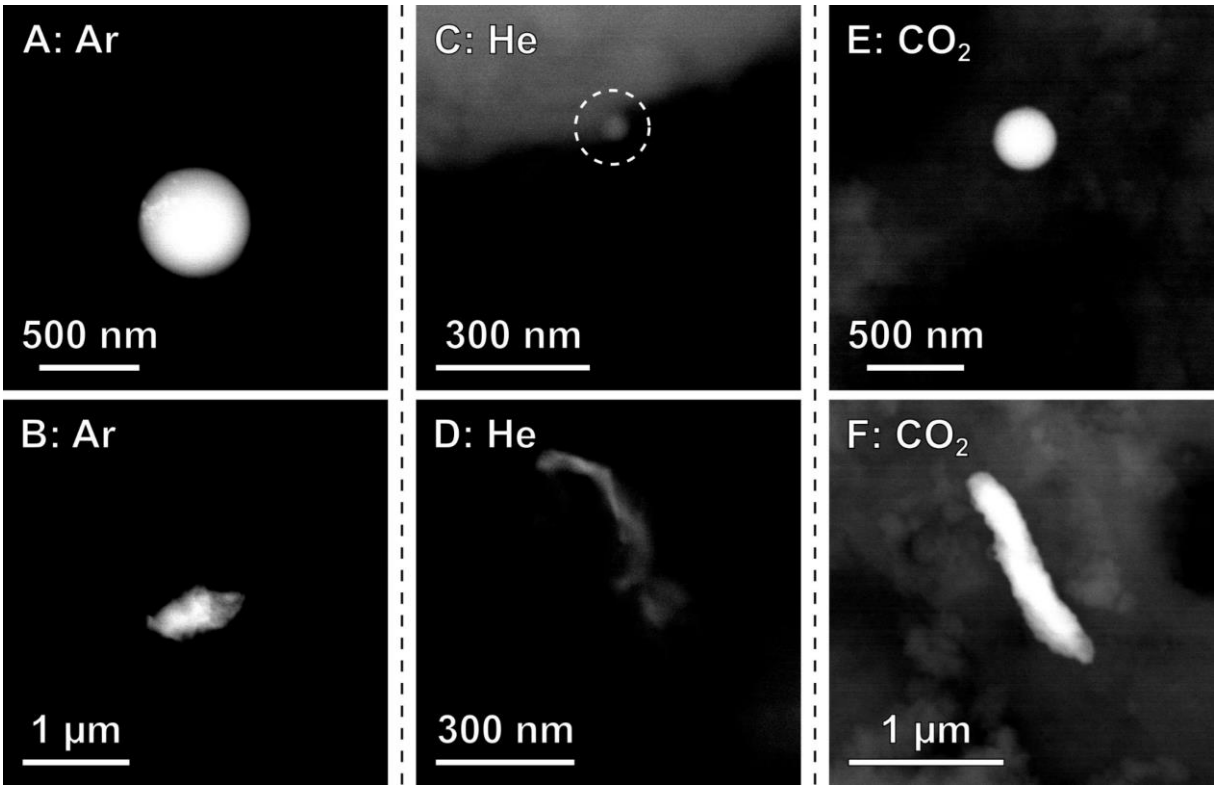

Figure 1: BSE-SEM images of the Ar (A-B), He (C-D), and CO_2 (E-F) samples. The BSE signal highlights the relatively heavy steel particles against the relatively light Al_2O_3 background. Particles with various morphologies were observed, though notably the Ar (A) and CO_2 (E) samples contained several highly spherical particles.

The SEM analyses enable the investigation of the overall morphology and the composition of the stainless steel particles. However, the SEM lacks the spatial resolution to study the surface structure of the steel particles, and may also miss smaller particles. Therefore, high-angle annular dark field scanning transmission electron microscopy (HAADF-STEM) was employed due to its higher spatial resolution compared to SEM. Furthermore, the HAADF signal scales with the projected density of the sample, highlighting the heavier steel particles against the lighter Al_2O_3 background. Figure 2 presents a representative overview of the particles that were observed in the Al_2O_3 samples exposed to the Ar

(A-B), He (C-D), and CO_2 (E-F) plasma (note that, again, all particles were confirmed to be stainless steel using EDX, consisting of Fe, Cr, and Ni; see SI, Section S2.2).

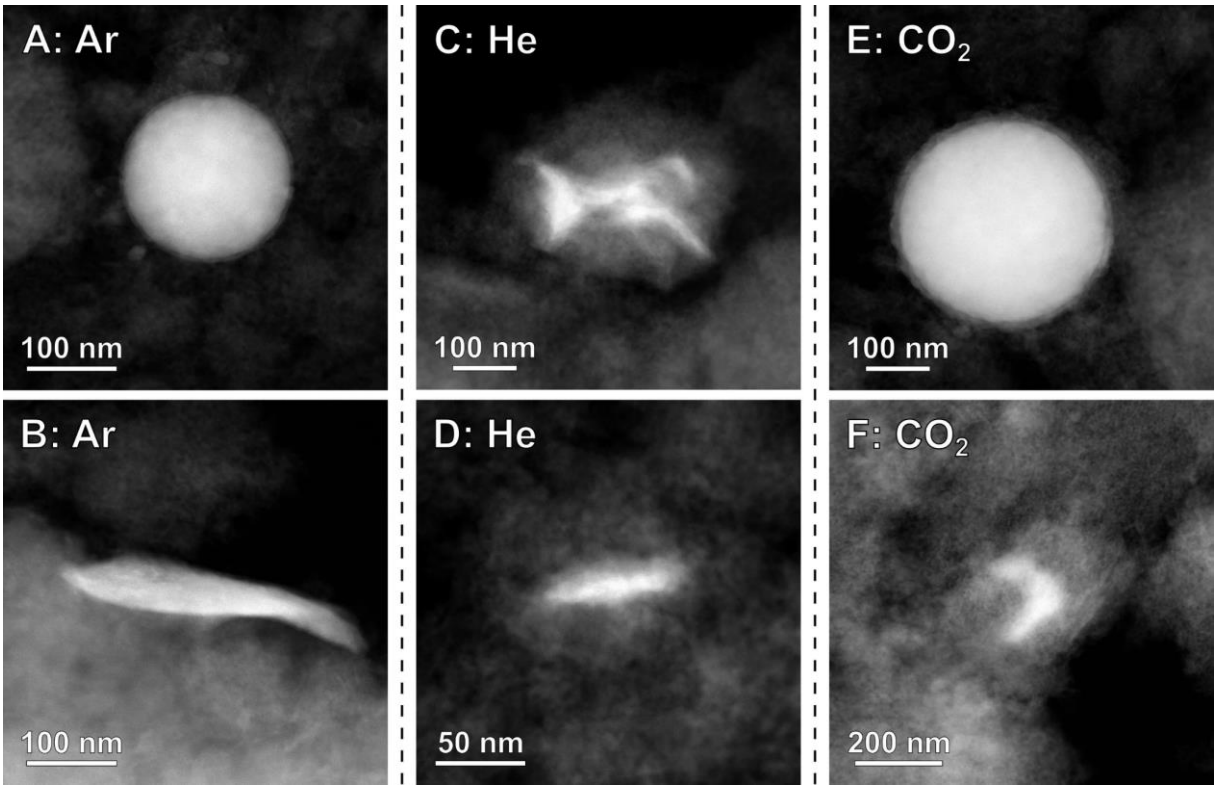

Figure 2: HAADF-STEM images of stainless steel particles in the Ar (A-B), He (C-D), and CO_2 (E-F) samples.

Based on the TEM images, particle size distributions could be determined. The particle size was defined as the diameter of the smallest circle that encompasses the entire stainless steel particle in the image. The histograms of these particle sizes are provided in Figure 3 A-C, whereas the fitted lognormal distributions are presented in Figure 3 D. Significant differences between the particle sizes from the various samples are observed (see SI Section S3 for more details). Indeed, the stainless steel particles from the He sample are generally much smaller than the others, and more narrowly distributed. The CO_2 sample has the broadest distribution, with the largest particles overall, while the Ar particle size distribution sits somewhere in between He and CO_2.

In addition to the particle size distributions, the increased spatial resolution of the TEM enables a more detailed investigation of the individual particles. Higher magnification TEM images in Figure 3 E (Ar) and F (CO_2) reveal that the spherical stainless steel particles have an oxide shell around their metallic core. Furthermore, the shell in the CO_2 sample is notable thicker compared to the Ar sample (10-15 nm versus 4-8 nm), which was observed for multiple spherical particles.

Despite the clear observations presented here, it should be noted that the absolute deposition quantity of the eroded particles is low. Bulk characterization techniques were unable to capture an increase in Fe, Cr, or Ni content, as the impurities present in the pristine spheres were too high, thus no change after the plasma was observed. Furthermore, it was challenging to objectively quantify the number of deposited particles based on e.g. the SEM measurements, as electron microscopy is inherently a local technique and the density of particles on the surface was low. In addition, the number of observed particles varied significantly between spheres, which is understandable as the plasma discharge is not homogeneous throughout the reactor and thus spheres in different locations will be affected

differently. This prevents a reliable measurement of the extent of the erosion in our current system. Nevertheless, the current data offer various insights and do enable a comparison between the various discharges.

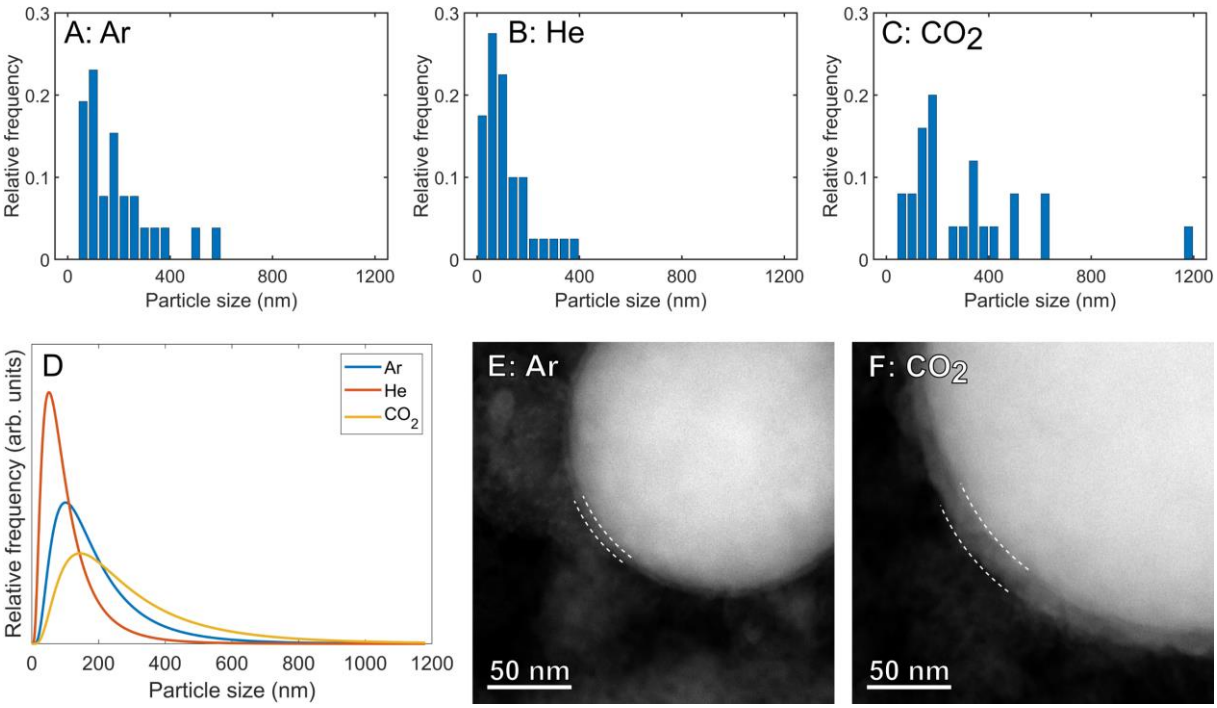

Figure 3: A-D: Particle size distributions for the stainless steel particles formed in the discharges in various gases, based on TEM data: A-C: Histograms of the particle sizes, for Ar (A: 26 particles), He (B: 40 particles) and CO_2 (C: 25 particles). D: Lognormal distributions. E, F: Higher magnification images of stainless steel spheres with a thin oxide shell, indicated by the dashed white lines for the Ar (E) and CO_2 (F) samples.

In order to understand what is causing the formation and deposition of these stainless steel particles, as well as which parameters influence the properties of these particles, the plasma discharge should be considered. Therefore, the plasma was electrically characterized, paying attention to two metrics we believe are highly relevant and representative for the discharge properties: the microdischarge quantity and the discharging areal fraction β. The microdischarge quantity is based on the Fourier transform of the plasma current signal, where the relevant frequency domain is integrated, yielding a value that includes contributions from both the number of microdischarges and their intensity (more details on this analysis can be found in[25]). The discharging areal fraction β is the fraction of the dielectric barrier actually participating in the discharge, and can be calculated based on the theoretical value of the dielectric capacitance and the measured charge-voltage diagrams (often called Lissajous figures).[25,26]

As presented in Figure 4, the plasma discharges in the different gases yield varying discharge characteristics. Representative voltage and plasma current signals of the discharge after 1 hour of operation are shown in Figure 4 A-C, whereas the measured Lissajous figures (also after 1 hour) are presented in Figure 4 D. Furthermore, the microdischarge quantity and discharging areal fraction were monitored over time, as presented in Figure 4 E and F, respectively. Both the visual inspection of the plasma current signal and the quantification of the microdischarges show that the CO_2 discharge is much more filamentary, with drastically more, and also more intense microdischarges. In addition, the Lissajous figure (in particular the inclination of the various edges, explained in detail in[26]) can be analyzed to reveal various discharge properties, such as the discharging areal fraction, as mentioned above. A discharging areal fraction β of less than 0.3 for the CO_2 discharge indicates that barely a

quarter of the dielectric barrier actually participates in the discharges. This implies that the power (which is slightly higher for the CO_2 discharge; see SI, section S4) is dissipated in a smaller volume compared to the discharges in Ar or He, leading to higher local power densities, as is also expected for filamentary discharges. In contrast, the He discharge exhibits opposite properties, both for the microdischarges and the discharging areal fraction β. Indeed, the He plasma yields almost no microdischarges, whereas β approaches 1, indicating that nearly the entire dielectric participates in the discharge and thus that the reactor is completely filled with plasma. The Ar plasma has a similar discharging areal fraction β as the He discharge, whereas it exhibits a more filamentary discharge at the start. During the first 1-2 hours of operation, the Ar discharge exhibits notably more microdischarges than the He discharge, though this behavior disappears over time. Note that although there are in fact changes in the discharge characteristics over time, they are not due to purely thermal effects. During the first ca. 30 minutes, the discharge characteristics can vary heavily, as can be expected due to heating of the system.[27] However, after again reaching the thermal steady state, the original trends of the discharge characteristics continue as before cooling down, indicating there must be an underlying, cumulative effect (more detailed graphs on the cumulative effects are presented in the SI, Section S5). This is also why the CO_2 plasma was operated for a longer time than the Ar and He plasma. The discharging areal fraction for Ar and He was already high from the start, and increased even more during the first hours of operation. A similar effect was hypothesized for CO_2, as the introduction of metal particles to the outside of the packing can have this effect,[25] but it was not observed immediately. Therefore, the plasma was operated for a longer time, to allow for the hypothesized cumulative effect to build up. However, even after these additional hours of plasma operation, this trend was not observed.

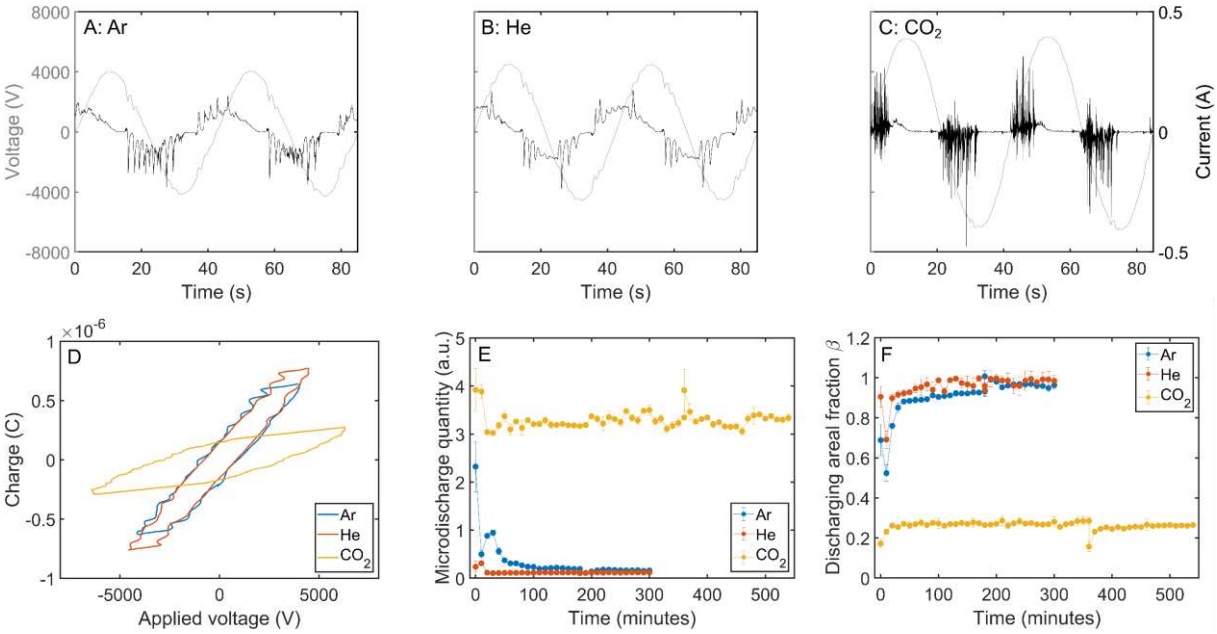

Figure 4: A-C: Representative voltage and plasma current signals after operating the plasma for 1 hour in Ar (A), He (B), and CO_2 (C). D: Representative Lissajous figures after operating the plasma for 1 hour for all gases. E: Microdischarge quantity over time for all gases. F: Discharging areal fraction β over time for all gases.

The quantification of the plasma discharge can offer valuable insights in the underlying mechanisms that are responsible for the formation of these stainless steel particles. For example, we believe that the abundance of the highly spherical particles observed by SEM (see also Figure 1) is directly related to the abundance and intensity of the microdischarges. Indeed, it was already shown by Nguyen-Smith et al. that the microdischarges are able to locally melt the electrode.[22] When a small amount of the

electrode melts locally, it is possible for a small droplet to be removed, after which it will quickly cool down and solidify (as it exits the high-intensity plasma region), thus forming these perfect spheres. This hypothesis is supported by our SEM observations, correlated with the plasma discharge characteristics. As demonstrated in Figure 4, the CO_2 plasma contained many intense microdischarges, leading to this high fraction of spherical steel particles. The Ar discharge was moderately filamentary, and only for a limited period of time, explaining why some spherical particles were found, but not many. Finally, the He discharge showed almost no microdischarges, which again corroborates with the lack of spherical particles.

Regardless of the discharge characteristics, non-spherical stainless steel particles were also observed in every sample. The more randomly shaped particles are most likely formed by different mechanisms, such as sputtering, for example. Ion energies in atmospheric pressure DBDs tend to be rather low, but there may still be ions with sufficient energy to remove material from the exposed electrode surface.[28–30] While ion mass may have some effect on the sputtering of a material, its influence is not trivial.[31,32] Moreover, although the molecular weight of CO_2 is slightly higher than that of Ar (44 g/mol versus 40 g/mol), it is unlikely that this can explain the differences in particle size distributions, as presented in Figure 3 A, especially since CO_2 molecules might split in lighter ions. Rather, the plasma discharge again appears to play a significant role. Indeed, the higher microdischarge quantity, in addition to the higher local power density, is likely intensifying the erosion mechanisms, yielding larger eroded particles for the CO_2 plasma compared to the others. Note that also other discharge parameters, such as burning voltage, frequency, and temperature, may also influence the erosion processes. In addition to sputtering, alternative or additional formation mechanisms for the steel particles caused by e.g., local heating, oxidation, or even explosive electron emission[33,34] cannot be ruled out.

Besides the physical effects causing the formation of these particles, chemical effects were also observed, as demonstrated in Figure 3 B-C by the stronger oxidation of the exterior of the steel spheres formed in the CO_2 plasma. Indeed, when the CO_2 plasma is sufficiently intense to locally melt the electrode, it is very likely that there will be reactive oxygen species present as well, causing oxidation of the outside layer of the stainless steel. In the Ar plasma, however, no oxygen should be present. Therefore, the lesser oxidation is attributed to oxidation in air during the manipulation of the spheres after plasma operation.

Although there is no direct evidence, oxidation of the steel particles in the CO_2 plasma may explain why the plasma discharge characteristics remained stable over the observed time, contrary to the Ar and He discharges. Indeed, the drop in microdischarge quantity and rise of the discharging areal fraction β is consistent with previous observations for the addition of metal particles to the exterior of the packing spheres, although the loading here is much lower.[25] If the exposed stainless steel particles on the spheres would all have oxide surfaces, this may explain why their impact on the plasma discharge is minimal, as the exposed oxide has very different properties than the metal. Though this is only a hypothesis, it does highlight the complexity of the system, making it very important to further our understanding of all processes taking place during the experiment.

It should be noted that, in addition to the materials described here, we also observed stainless steel particles on the packing material after plasma operation for other DBD reactors with very different specifications (see SI, Section S6, including a sample from[35]). Moreover, very small nanoparticles (down to 2-3 nm) were found in a carbon matrix after generating a pure CH_4 plasma in an empty DBD (see SI, Section S7). Hence, despite the large variety in reactor geometries and operating conditions, the erosion and subsequent deposition of an exposed metal electrode in a DBD seems inevitable. Therefore, it is crucial that this phenomenon is known and understood. Whether this effect is

problematic, or to what extent, depends heavily on the desired application. For example, when treating biological samples, such as seeds or even food, a small number of metal nanoparticles may already pose toxicity risks.[36] In addition, when treating or synthesizing materials using DBDs, the deposition of these particles may introduce undesired impurities. Also in plasma catalysis, this effect may be drastic, especially when considering long-term operation with the aim of further upscaling and industrialization. Indeed, as discussed earlier, the deposition of metal particles on the packing material is likely to have an effect on the discharge characteristics, which in turn will alter the overall performance. Moreover, the introduction of (overlooked) metal(oxide) particles may offer catalytically active sites, that could further steer the reactions in a different direction over time. Therefore, it is crucial that researchers are aware of this effect, so it can be taken into account when interpreting results and designing novel systems. Note that this issue could be addressed by employing a double DBD, where both electrodes are covered by a dielectric. Although this would prevent the formation and deposition of steel particles, the dielectric material may erode to some extent as well, as was recently shown by Wang et al. for surface DBDs.[21] Moreover, covering the second electrode will alter the plasma discharge, which may limit the overall performance of the system.[37] Whether the use of a double DBD is beneficial depends on the precise application, finding a balance between the deposition of the electrode material and the alteration of the discharge, with potential effects on the overall performance.

In conclusion, while dielectric barrier discharges (DBDs) are generally regarded as gentle plasmas, our study demonstrates that the exposed stainless steel electrodes undergo erosion. This erosion leads to the deposition of stainless steel particles on the packing material, becoming a significant source of contamination. Our results indicate that the plasma discharge parameters strongly influence the particles' size, shape, and surface oxidation, yet the formation of these particles occurs consistently across different operating conditions, suggesting this issue is widespread.

The presence of these particles must be considered in all potential applications, such as material synthesis or functionalization. In catalytic applications, stainless steel particle contamination may obscure experimental results and ultimately affect the plasma discharge, thereby impacting overall performance. Additionally, when DBD plasmas are used for treating biological systems like seeds or food, the presence of stainless steel particles could pose serious health risks, emphasizing the importance of understanding and mitigating this effect in practical applications.

Supporting Information

Experimental method details, energy dispersive X-ray spectra, details on the fit of the particle size distributions, plasma power over time, discharge characteristics over time, data on steel particles from other reactors, steel particles in a carbon matrix formed in an empty reactor

Acknowledgements

The authors acknowledge Joran Van Turnhout and Rani Vertongen for kindly providing us with the additional samples they used in their different reactors.

This research was supported through long-term structural funding (Methusalem FFB15001C) and by the European Research Council (ERC) under the European Union's Horizon 2020 research and innovation programme with grant agreement No 810182 (SCOPE ERC Synergy project) and with grant agreement No 815128 (REALNANO).

References

1. Fridman, A. & Kennedy, L. *Plasma Physics and Engineering*. (2016).
2. Borcia, G., Anderson, C. A. & Brown, N. M. D. Dielectric barrier discharge for surface treatment: application to selected polymers in film and fibre form. *Plasma Sources Sci. Technol.* **12**, 335–344 (2003).
3. Wagner, H.-E. *et al.* The barrier discharge: basic properties and applications to surface treatment. *Vacuum* **71**, 417–436 (2003).
4. Lapena, M. H. & Lopes, C. M. A. Improvement of aerospace thermoplastic composite adhesion to coating with dielectric barrier discharge atmospheric pressure plasma surface treatment. *Plasma Processes & Polymers* **20**, 2200081 (2023).
5. Mierczynski, P., Mierczynska-Vasilev, A., Szynkowska-Jozwik, M. & Vasilev, K. Atmospheric plasma in the preparation and pre-treatment of catalytic materials – A mini review. *Catalysis Communications* **187**, 106839 (2024).
6. Wang, Z. *et al.* Catalyst Preparation with Plasmas: How Does It Work? *ACS Catal.* **8**, 2093–2110 (2018).
7. Khoja, A. H., Tahir, M. & Amin, N. A. S. Cold plasma dielectric barrier discharge reactor for dry reforming of methane over Ni/ɣ-Al2O3-MgO nanocomposite. *Fuel Processing Technology* **178**, 166–179 (2018).
8. He, J. *et al.* Dielectric barrier discharge plasma for nanomaterials: Fabrication, modification and analytical applications. *TrAC Trends in Analytical Chemistry* **156**, 116715 (2022).
9. HafezKhiabani, N., Fathi, S., Shokri, B. & Hosseini, S. I. A novel method for decoking of Pt–Sn/Al2O3 in the naphtha reforming process using RF and pin-to-plate DBD plasma systems. *Applied Catalysis A: General* **493**, 8–16 (2015).
10. Kim, M., Jeoung, J., Kim, J. & Ha, K.-S. Regeneration of deactivated H-ZSM-5 for aromatization by dielectric barrier discharge plasma. *Applied Catalysis A: General* **575**, 214–222 (2019).

11. Bogaerts, A. *et al.* The 2020 plasma catalysis roadmap. *Journal of Physics D: Applied Physics* **53**, 443001 (2020).
12. Ollegott, K., Wirth, P., Oberste-Beulmann, C., Awakowicz, P. & Muhler, M. Fundamental Properties and Applications of Dielectric Barrier Discharges in Plasma-Catalytic Processes at Atmospheric Pressure. *Chemie Ingenieur Technik* **92**, 1542–1558 (2020).
13. Bogaerts, A., Neyts, E. C., Guaitella, O. & Murphy, A. B. Foundations of plasma catalysis for environmental applications. *Plasma Sources Sci. Technol.* **31**, 053002 (2022).
14. Nishime, T. M. C., Wannicke, N., Horn, S., Weltmann, K.-D. & Brust, H. A Coaxial Dielectric Barrier Discharge Reactor for Treatment of Winter Wheat Seeds. *Applied Sciences* **10**, 7133 (2020).
15. Roy, S., Choudhury, B., Johnson, J. & Schindler-Tyka, A. Application of dielectric barrier discharge for improving food shelf life and reducing spoilage. *Sci Rep* **11**, 19200 (2021).
16. Laroque, D. A., Seó, S. T., Valencia, G. A., Laurindo, J. B. & Carciofi, B. A. M. Cold plasma in food processing: Design, mechanisms, and application. *Journal of Food Engineering* **312**, 110748 (2022).
17. Daeschlein, G. *et al.* Skin decontamination by low-temperature atmospheric pressure plasma jet and dielectric barrier discharge plasma. *Journal of Hospital Infection* **81**, 177–183 (2012).
18. Brandenburg, R. Dielectric barrier discharges: progress on plasma sources and on the understanding of regimes and single filaments. *Plasma Sources Sci. Technol.* **26**, 053001 (2017).
19. Hanson, R. E., Houser, N. M. & Lavoie, P. Dielectric material degradation monitoring of dielectric barrier discharge plasma actuators. *Journal of Applied Physics* **115**, 043301 (2014).
20. Bian, D., Wu, Y., Long, C. & Lin, B. Effects of material degradation on electrical and optical characteristics of surface dielectric barrier discharge. *Journal of Applied Physics* **124**, 183301 (2018).
21. Wang, A. *et al.* The time evolution of electrical and thermodynamic characteristics of surface dielectric barrier discharge caused by dielectric degradation. *J. Phys. D: Appl. Phys.* **57**, 445203 (2024).

22. Nguyen-Smith, R. T. *et al.* μs and ns twin surface dielectric barrier discharges operated in air: from electrode erosion to plasma characteristics. *Plasma Sources Sci. Technol.* **31**, 035008 (2022).
23. Selivonin, I., Lazukin, A., Moralev, I., Krivov, S. & Roslyakov, I. Erosion of the sputtered electrodes in the surface barrier discharge. *J. Phys.: Conf. Ser.* **1394**, 012027 (2019).
24. Selivonin, I. & Moralev, I. Microdischarges properties in sDBD: the role of the exposed electrode oxidation. *Plasma Sources Sci. Technol.* **30**, 035005 (2020).
25. De Meyer, R. *et al.* Importance of plasma discharge characteristics in plasma catalysis: Dry reforming of methane vs. ammonia synthesis. *Chemical Engineering Journal* **488**, 150838 (2024).
26. Peeters, F. J. J. & van de Sanden, M. C. M. The influence of partial surface discharging on the electrical characterization of DBDs. *Plasma Sources Science and Technology* **24**, 015016 (2014).
27. Ráhel, J., Szalay, Z., Čech, J. & Morávek, T. On spatial stabilization of dielectric barrier discharge microfilaments by residual heat build-up in air. *Eur. Phys. J. D* **70**, 92 (2016).
28. Neyts, E. C. Plasma-Surface Interactions in Plasma Catalysis. *Plasma Chem Plasma Process* **36**, 185–212 (2016).
29. Babaeva, N. Y. & Kushner, M. J. Ion energy and angular distributions onto polymer surfaces delivered by dielectric barrier discharge filaments in air: I. Flat surfaces. *Plasma Sources Sci. Technol.* **20**, 035017 (2011).
30. Babaeva, N. Y., Ning, N., Graves, D. B. & Kushner, M. J. Ion activation energy delivered to wounds by atmospheric pressure dielectric-barrier discharges: sputtering of lipid-like surfaces. *J. Phys. D: Appl. Phys.* **45**, 115203 (2012).
31. Yamamura, Y. & Tawara, H. Energy dependence of ion-induced sputtering yields from monatomic solids at normal incidence. *Atomic Data and Nuclear Data Tables* **62**, 149–253 (1996).
32. Mauchamp, N. A. & Hamaguchi, S. Why are physical sputtering yields similar for incident ions with different masses?—physical sputtering yields of the Lennard–Jones system. *J. Phys. D: Appl. Phys.* **55**, 225209 (2022).

33. Mesyats, G. A. Ecton mechanism of the vacuum arc cathode spot. *IEEE Trans. Plasma Sci.* **23**, 879–883 (1995).
34. Mesyats, G. A. Ecton Mechanism of the Cathode Spot Phenomena in a Vacuum Arc. *IEEE Trans. Plasma Sci.* **41**, 676–694 (2013).
35. Vertongen, R. *et al.* Sorption-Enhanced Dry Reforming of Methane in a DBD Plasma Reactor for Single-Stage Carbon Capture and Utilization. *ACS Sustainable Chem. Eng.* **12**, 10841–10853 (2024).
36. Egbuna, C. *et al.* Toxicity of Nanoparticles in Biomedical Application: Nanotoxicology. *Journal of Toxicology* **2021**, 1–21 (2021).
37. Mei, D. *et al.* CO2 reforming of CH4 in single and double dielectric barrier discharge reactors: Comparison of discharge characteristics and product distribution. *Journal of CO2 Utilization* **53**, 101703 (2021).

Supporting information

Contamination in dielectric barrier discharge plasmas by electrode erosion

Robin De Meyer[1, 2, 3], Jo Verbeeck[2], Sara Bals[2, 3,*] and Annemie Bogaerts[1,*]

[1] *Research group PLASMANT, Department of Chemistry, University of Antwerp, Universiteitsplein 1, 2610 Antwerp, Belgium*
[2] *Research group EMAT, Department of Physics, University of Antwerp, Groenenborgerlaan 171, 2020 Antwerp, Belgium*
[3] *Nanolab Centre of Excellence, University of Antwerp, Groenenborgerlaan 171, 2020 Antwerp, Belgium*

** corresponding author: annemie.bogaerts@uantwerpen.be*
** corresponding author: sara.bals@uantwerpen.be*

Contents

S1. Experimental Methods

S1.1. DBD reactor schematic and technical details

The experimental setup is schematically presented in Figure S1, including the precise dimensions of the reactor. The gases (Air Liquide; Ar ≥ 99.999 %, He ≥ 99.999 %, CO_2 ≥ 99.998 %) were controlled by a mass flow controller (Bronkhorst). The plasma was generated using the G10 S-V AFS GmbH power supply unit (PSU) set at 23.5 kHz, while the discharge was monitored using a high voltage probe (Tektronix P6015A), a current monitor (Pearson Electronics 4100, high-frequency 3 dB point approx. 35 MHz), and a low voltage probe (Pico Technology TA150) across a 10 nF monitoring capacitor. All probes were connected to a Picoscope 6402A (Pico Technology, bandwidth 250 MHz) oscilloscope that was used to save snapshots of the discharge for later analysis. The inner electrode of the reactor is made of 304 stainless steel, while the dielectric barrier consists of alumina (Al_2O_3). The reactor was packed with pristine γ-Al_2O_3 spheres (Sasol) with a diameter of 1.8 mm prior to each experiment. This setup was previously described and characterized in detail in [1].

The gas flow rate was set at 100 mls/min with a constant applied power, yielding a relatively stable plasma power of 45-50 W for Ar and He, and around 60-65 W for the CO_2 discharge, as presented in Section S4.

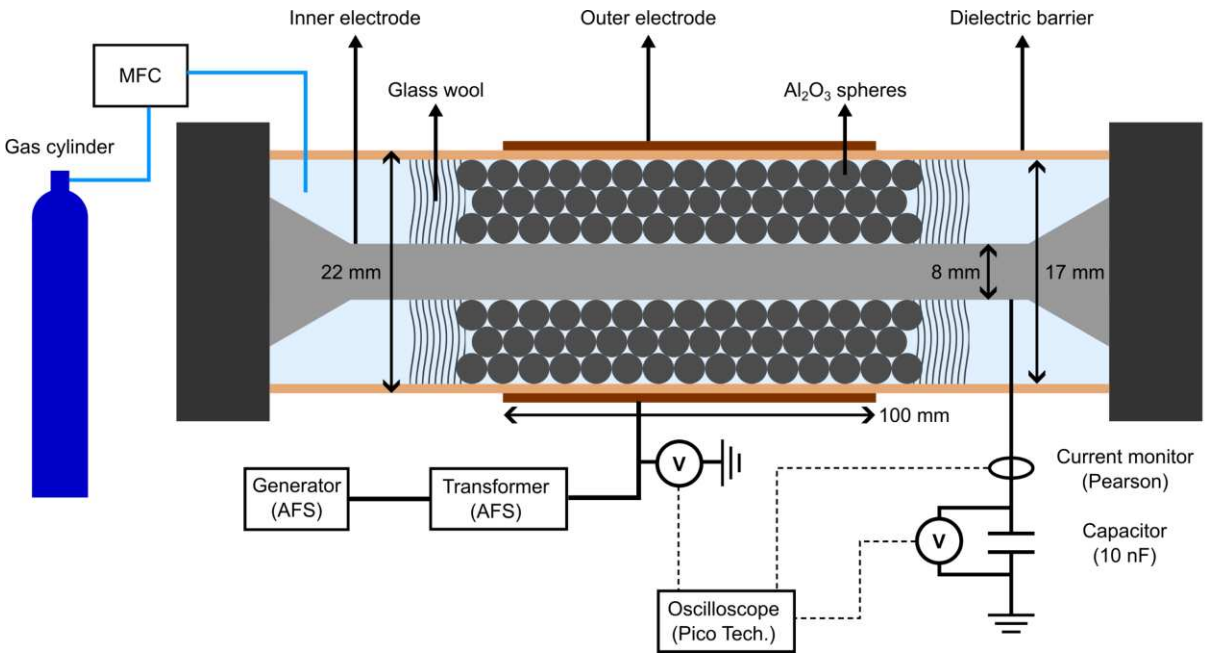

Figure S1: Schematic of the complete experimental setup including reaction dimensions. This figure is an adapted version of a figure that was previously published in[1].

S1.2. SEM and TEM parameters

S1.2.1. SEM

For the SEM analyses, a Thermo Fisher Scientific Quanta 250 ESEM was employed. An acceleration voltage of 20 kV was used, with a working distance of 10 mm, while operating the microscope in its high vacuum mode. The built-in Everhart-Thornley (secondary electron, SE) detector, as well as the pole piece-mounted backscattered electron (BSE) detector were used. An Oxford Instruments energy dispersive and wave dispersive X-ray detector were used to identify three key elements in the particles of interest: Fe, Cr, Ni. Both detectors were used at some point, depending on technical operability of the detectors at the time of the various analyses.

Prior to the analyses, entire spheres were attached to a SEM stub using silver paint, after which the exposed surfaces of the spheres were coated with approximately 25 nm of carbon to improve surface conductivity.

S1.2.2. TEM

The TEM analyses were performed using a Thermo Fisher Scientific Tecnai Osiris microscope operated at 200 kV, with a camera length of 115 mm. HAADF-STEM imaging and EDX-STEM analyses were performed to identify and investigate the stainless steel particles. A beam current of approximately 125 pA was used. Prior to the TEM analyses, 5 spheres were added to a vial with approximately 1 ml of acetone, after which the sample was vortexed and sonicated for around 30 seconds each. Next, a few drops of the resulting liquid were dropcast on a holey carbon TEM support grid, which was left to dry in ambient conditions.

For the bright field TEM analysis of the steel particles in a carbon matrix (Figure S9 C below), the same microscope was used, operated at 200 kV in conventional brightfield TEM imaging mode. A small amount of the material formed in the reactor was added to a vial and sonicated together with a few drops of acetone. Then, a few drops of this suspension were dropcast on a holey carbon grid, prior to TEM analysis.

S1.2.3. A note on bias

For the SEM analyses, the spheres were manipulated minimally, ensuring a maximally representative sample in the SEM. However, the experimental conditions were challenging. Indeed, stainless steel particles, usually just hundreds of nm large, were scattered across an Al_2O_3 sphere of almost 2 mm in diameter. In addition, the concentration of particles was low. This meant that large areas of the sphere had to be searched for few and small particles. Due to the presence of impurities in the pristine Al_2O_3 spheres, automating this process proved challenging. Therefore, it is likely that the actual data acquired is somewhat biased, most likely towards larger particles, as they would stand out more against the lighter background. Furthermore, the SEM may also have been resolution-limited, especially when screening areas at a relatively low magnification, possibly further biasing the data. However, as all samples were treated and analyzed in the same way, we believe relative comparisons between the samples are still highly relevant. For the TEM analyses, a similar bias towards larger particles may be expected. However, in addition, the samples were manipulated quite drastically in order to be able to analyze the stainless steel particles themselves. It is plausible that in this process, a sort of pre-selection of stainless steel particles was made, as some particles may have stronger or weaker interactions with the support than others, thus potentially introducing another bias to the analyses. However, again, since all samples were manipulated and analyzed using an identical approach, a relative comparison should still be valid. Though, due to the differences in sample manipulation, a direct comparison between SEM and TEM data may be less justified.

S2. Representative EDX spectra

S2.1. SEM-EDX

A representative SEM-EDX spectrum is presented in Figure S2. The spectrum shows strong O and Al signals, which makes sense given that the particle was on an Al_2O_3 sphere during analysis. Indeed, when employing SEM-EDX for such relatively small particles, the primary electron beam interacts with a larger volume than just the particle of interest in this case, yielding the strong O and Al signals. However, when highlighting the relevant energy range, clear signals for Fe, Cr, Ni, and even Mn were also observed, thus confirming the composition of the stainless steel particle.

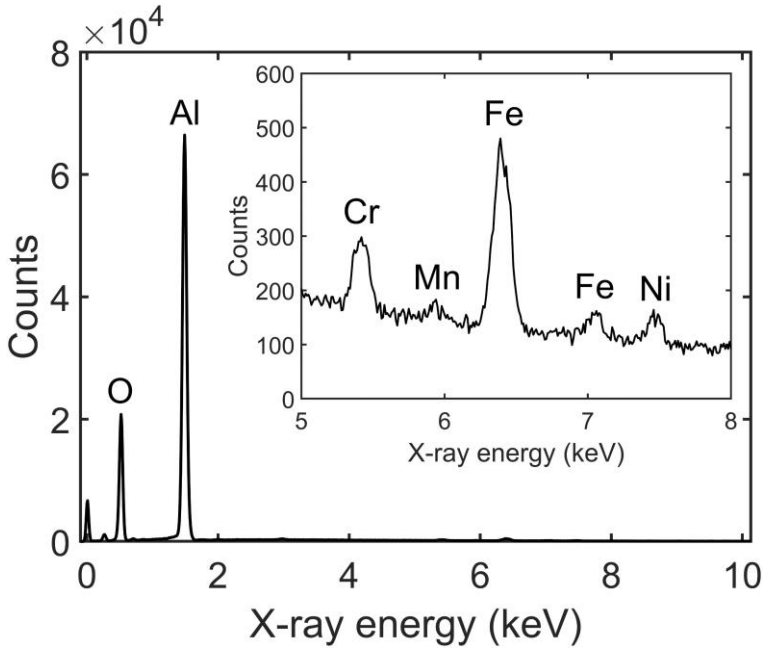

Figure S2: Representative SEM-EDX spectrum from a stainless steel particle on the surface of an Al_2O_3 sphere, used in the Ar plasma. Strong Al and O peaks are present due to the Al_2O_3 support, while Fe, Cr, and Ni could be observed, confirming the composition of the stainless steel particle.

S2.2. TEM-EDX

In Figure S3, a representative EDX spectrum as obtained in the TEM is presented. The composition of the particles can again be confirmed by identifying the Fe, Cr, Ni, and Mn signals, clearly indicating that the particle is stainless steel. In addition to these elements, Al and O were again observed as they make up the Al_2O_3 support material that was still present during TEM analysis, though the peaks are not as dominant due to the different geometry compared to the SEM. Finally, also Cu and C signals were observed, but these can be attributed to the support on which the sample was deposited for TEM analysis.

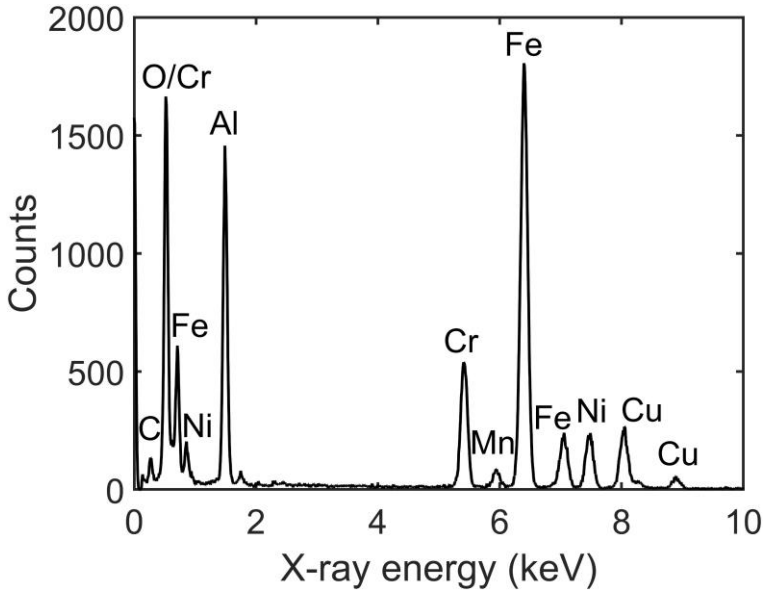

Figure S3: Representative TEM-EDX spectrum for a stainless steel particle, extracted from an Al_2O_3 sphere that was exposed to the CO_2 plasma. The identifying elements for stainless steel (Fe, Cr, Ni) are clearly present. In addition, Cu and C signals were also observed, but these can be attributed to the TEM support on which the sample was deposited.

S3. Particle size distribution fits

The histograms presenting the measured particle sizes are shown in Figure 3 of the main text, as well as lognormal fits of these data. A Lilliefors test for normality was performed on the logarithms of the particle sizes of each sample. For every dataset, the Lilliefors test accepted the null hypothesis that the data comes from a normal distribution, justifying the lognormal fit. Furthermore, two-sample t-tests revealed significant differences between the different sets of logarithmic values, proving that there is a significant difference between the various particle size distributions.

S4. Plasma power over time

The plasma power was determined at every timestep (average of three snapshots), and is presented in Figure S4. After the initial thermal stabilization, the plasma power remains quite stable over time, though a slight decreasing trend may be observed for the CO_2 plasma. Despite being operated at the same "PSU power", i.e., the power set on the power supply (100 W), the actual plasma powers differ significantly. The plasma power for the Ar and He discharge are (after thermal stabilization) 45-50 W, while the plasma power for the CO_2 discharge is 60-65 W.

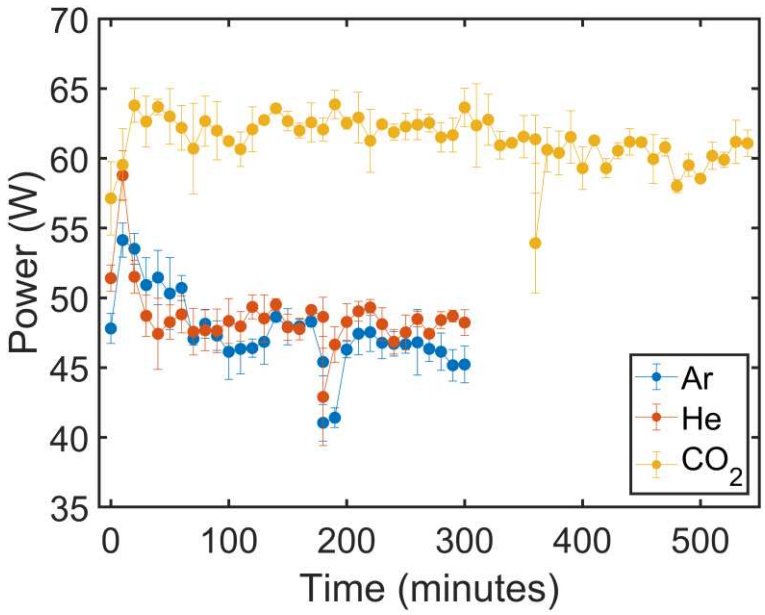

Figure S4: Plasma power over time for all gases.

S5. Discharge characteristics and thermal effect

The discharging areal fraction β and microdischarge quantity over time are presented below, for the Ar (Figure S5), He (Figure S6), and CO_2 (Figure S7) discharge. Note that the y-axes are different to reveal the details of the data, while major difference may be present between the different gases. The orange data points indicate the second phase of each experiment, so after reignition once cooled down to room temperature. In most cases, the first half hour shows some additional variation of the values due to heating of the system, but after that, the trend from the end of the first phase continues. Only the discharging areal fraction during the CO_2 discharge appears to reach the previous value slightly slower, but is still very near those values. These results indicate that, especially for the Ar and He discharges, there is a cumulative effect independent of the temperature, i.e., something is changing in the system, that is causing the plasma discharge characteristics to vary slightly.

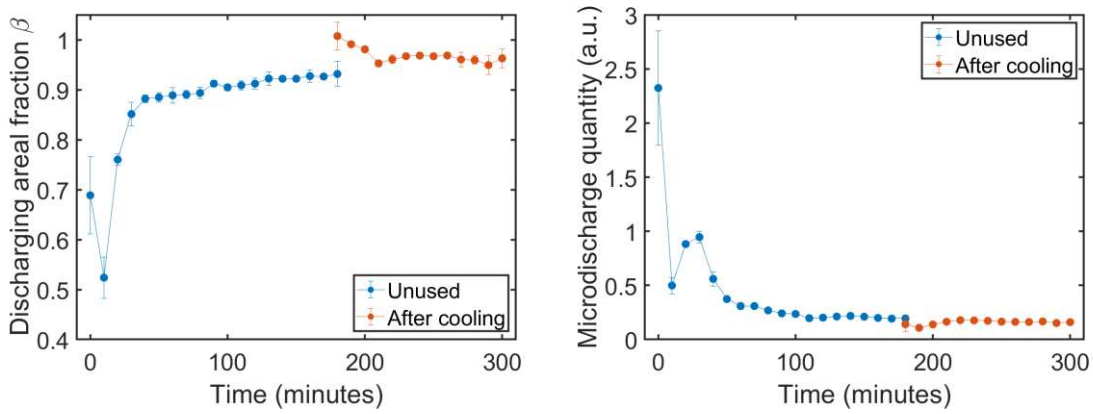

Figure S5: Discharging areal fraction β (left) and microdischarge quantity (right) during the Ar discharge. The orange data points indicate the data after cooling down. The increasing trend of the discharging areal fraction continues after thermal stabilization upon reigniting the plasma, and the same goes for the decreasing trend of the microdischarge quantity.

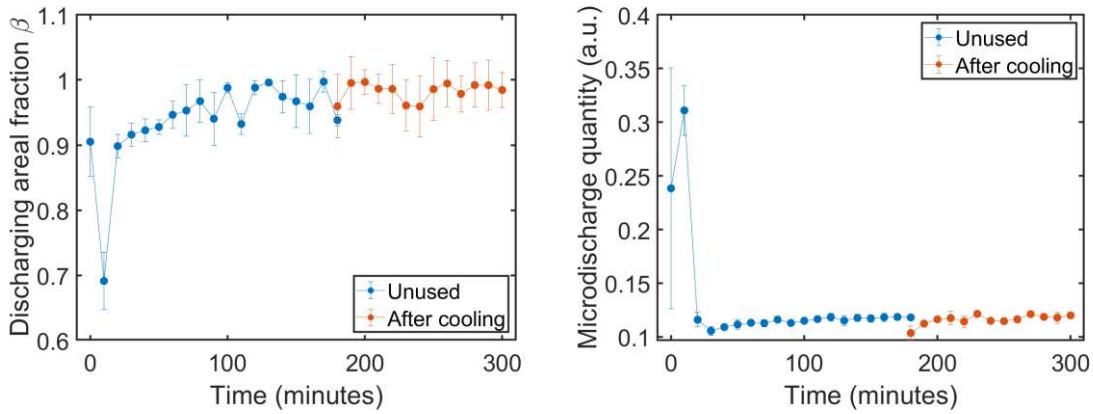

Figure S6: Discharging areal fraction β (left) and microdischarge quantity (right) during the He discharge. The orange data points indicate the data after cooling down. The large variations after the initial ignition are not observed upon reigniting the plasma after cooling down.

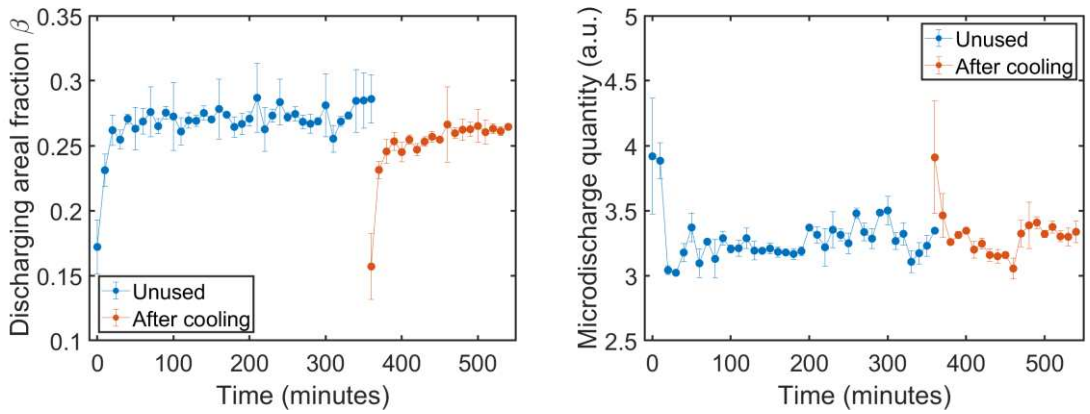

Figure S7: Discharging areal fraction β (left) and microdischarge quantity (right) during the CO_2 discharge. The orange data points indicate the data after cooling down. No clear cumulative effect is observed, and similar behavior can be found after reignition compared to the initial ignition.

S6. Samples used in other DBD reactors

Two additional spent packing materials that were used in completely different packed-bed DBDs and operated under different conditions were kindly provided for additional analyses. These samples were analyzed by SEM and energy dispersive X-ray spectroscopy (EDX) to investigate whether they also contained stainless steel particles. While both additional samples were used in distinctly different reactors, they all have an exposed stainless steel central electrode in common. Our analyses revealed that both additional samples also contained stainless steel particles, and examples are presented in Figure S8. Their composition was again confirmed by EDX. The technical specifications of the reactors used are provided in Table S1. It is clear that they span a wide range of properties, highlighting that this phenomenon is not unique to a particular system.

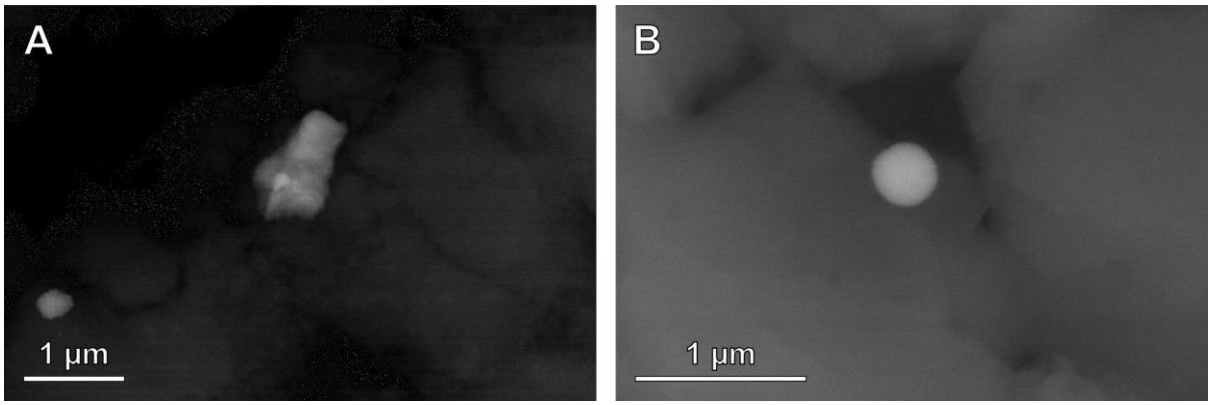

Figure S8: BSE-SEM images of stainless steel particles found on a silica (A) and zeolite 5A (B) support after being used in a packed-bed DBD experiment.

Table S1: Specifications of the packed-bed DBD reactors in which the presented samples were used.

Packing material	**alumina (this work)**	**silica**	**zeolite 5A**[2]
Discharge gap (mm)	4.5	2.5	1
PSU frequency (kHz)	23.5	23.5	45
Plasma power (W)	45-65	ca. 25	ca. 30
Dielectric material	alumina	glass (water cooled)	alumina
Inner electrode material	stainless steel	stainless steel	stainless steel
Discharge gas	Ar, He, or CO_2	$CO_2 + H_2$	$CO_2 + CH_4 + Ar$

S7. Steel particles in carbon matrix formed in CH_4 plasma

The same reactor that was used for the silica sample from Section S6 was used empty to generate a pure CH_4 plasma. After operating the plasma continuously for 2 h with a plasma power of ca. 25 W, carbon deposits were collected and analyzed. The SEM and TEM data are presented in Figure S9. All data clearly illustrate the presence of steel particles on and throughout the carbon material. The brightfield TEM analyses even revealed very small particles, down to 2-3 nm. The representative SEM-EDX spectrum again confirms that the particles are indeed stainless steel.

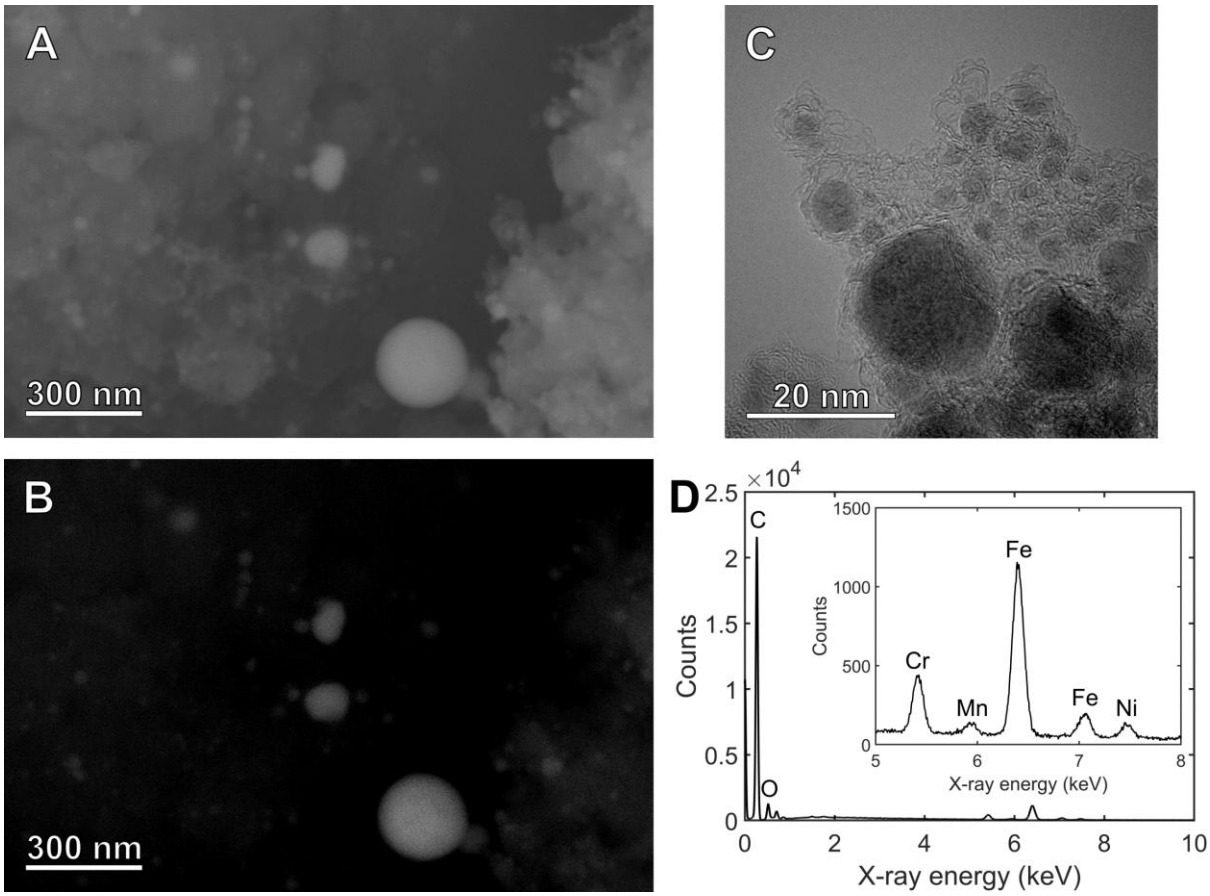

Figure S9: A, B: SE- (A) and BSE- (B) SEM images of the carbon deposits that were generated in the empty DBD with a CH_4 plasma. Heavy (steel) particles are clearly present in the carbon material. C: Brightfield TEM image of steel nanoparticles inside the carbon material. D: Representative SEM-EDX spectrum of the heavy particles in the carbon material, clearly containing Fe, Cr, and Ni, identifying the particles as stainless steel.

S8. References

(1) De Meyer, R.; Gorbanev, Y.; Ciocarlan, R.-G.; Cool, P.; Bals, S.; Bogaerts, A. Importance of Plasma Discharge Characteristics in Plasma Catalysis: Dry Reforming of Methane vs. Ammonia Synthesis. *Chemical Engineering Journal* **2024**, *488*, 150838. https://doi.org/10.1016/j.cej.2024.150838.

(2) Vertongen, R.; De Felice, G.; Van Den Bogaard, H.; Gallucci, F.; Bogaerts, A.; Li, S. Sorption-Enhanced Dry Reforming of Methane in a DBD Plasma Reactor for Single-Stage Carbon Capture and Utilization. *ACS Sustainable Chem. Eng.* **2024**, *12*, 10841–10853. https://doi.org/10.1021/acssuschemeng.4c02502.